THE ASTRONOMICAL JOURNAL VOLUME 95, NUMBER 3 MARCH 1988

LOCAL SIMULATIONS OF PLANETARY RINGS

JACK WISDOM
Department of Earth, Atmospheric, and Planetary Sciences, Massachusetts Institute of Technology, Cambridge, Massachusetts 02139

SCOTT TREMAINE
Canadian Institute for Theoretical Astrophysics, University of Toronto, Toronto, Ontario M5S 1A1, Canada
Received 1 October 1987; revised 16 November 1987

ABSTRACT

We present a new numerical method for studying the equilibrium properties of planetary rings, in which a small patch of the ring is simulated with periodic boundary conditions. The results of the simulations compare favorably with the results of kinetic theory of dense fluids so long as the filling factor in the midplane is less than about 0.5. The conclusion of Araki and Tremaine (1986) that the condition for the viscous instability is not fulfilled is confirmed. We find that the "standard" ring model, with the particles all of the same size, develops vertically stratified layers at large optical depths ($\tau \gtrsim 1$) when mean self-gravity is included.

I. INTRODUCTION

What shall we say to a great stratum of rubbish jostling and jumbling round Saturn without hope of rest or agreement in itself...

Maxwell (1857)

Despite recent advances in our understanding of the dynamics of planetary rings, much of the structure that is observed in the Saturnian ring system remains unexplained. The B ring, in particular, exhibits large irregular variations in optical depth that are not associated with any resonances with known satellites. The presence of this irregular structure is surprising because the timescale on which such irregularities should be removed by viscous diffusion is much shorter than the age of the solar system. A principal candidate mechanism to explain this irregular structure has been the "visocus instability" of Lin and Bodenheimer (1981), Lukkari (1981), and Ward (1981). The instability arises if the viscous stress is lower in regions of high surface density or optical depth. Material then migrates to regions of high optical depth from regions of lower optical depth, leaving annular bands of contrasting density. A condition for this instability is that the product of the optical depth τ and the height-averaged kinematic ring viscosity $\bar{\nu}$ must decrease with increasing optical depth over some interval of optical depth. The velocity-dependent coefficient of restitution found in the experiments of Bridges, Hatzes, and Lin (1984) on low-velocity collisions of icy spheres seemed to confirm that the $\tau\bar{\nu}$ condition for the viscous instability was indeed satisfied, on the basis of the relationship between the coefficient of restitution and the viscosity for a dilute gas of inelastic spheres. However, it is likely that the ring is not dilute, in other words, that the fraction of the ring volume occupied by the ring particles (the "filling factor" or "solid fraction") is not small compared to unity. In this case there is a significant new contribution to the viscous stress, corresponding to momentum transport through sound waves in the ring particles (the "nonlocal" viscosity). Araki and Tremaine (1986) argued that, when nonlocal viscosity is taken into account, the $\tau\bar{\nu}$ condition for the viscous instability is no longer satisfied, at least in the models they examined.

Several alternate mechanisms for producing the fine-scale structure of the B ring have been suggested. Borderies, Goldreich, and Tremaine (1985) and Araki and Tremaine (1986) pointed out that if the filling factor is as large as ~ 0.5 there might be a liquid–solid "phase transition," in which local patches or radial annuli of the ring behave like a solid rather than a fluid. Similar behavior is common in granular shear flow and is known as "plug" flow. However, axisymmetric solid rings are not in dynamical equilibrium unless there is adhesion between the ring particles or confining pressure from adjacent regions in which the ring is liquid. Thus, although the liquid–solid phase transition is known to occur at a filling factor of 0.48 in a stationary hard-sphere fluid, it is not known whether a similar transition occurs in a shearing ring.

Another possibility is that the B ring structure is a consequence of unstable density waves. Borderies *et al.* (1985) used a simple heuristic model of the viscous stress in a dense ring to establish that density waves could be unstable (this can be regarded as a viscous overstability, in contrast to the viscous instability discussed earlier). They predicted that standing waves generated by this internal overstability might be present in narrow rings, a prediction that is consistent with the subsequent discovery of an $m = 2$ normal mode in the Uranian δ ring and an $m = 0$ mode in the γ ring (French *et al.* 1987).

Explanations of the fine-scale structure of the B ring can be divided into two general classes: those that involve long-range gravitational forces between the ring particles (such as unstable waves), and those that involve only short-range forces arising through direct collisions (such as the liquid–solid phase transition). In this paper we concentrate on theories of the second class. More explicitly, we investigate the behavior of disks composed of inelastic, smooth, spherical particles, all of the same size, orbiting in a Keplerian force field (this is sometimes called the "standard model" of planetary rings). More complicated models, involving a distribution of particle sizes, rough or nonspherical particles, can be investigated by straightforward extensions of the techniques described here.

Studies of the standard model so far have largely been pursued in the context of kinetic theory, where numerous statistical assumptions must be made. For instance, theories based on the Boltzmann equation assume that successive collisions are uncorrelated ("molecular chaos"), that the phase-space distribution function is adequately represented by products of single particle distribution functions, and that only binary collisions are important. To simplify the analysis, additional assumptions are usually made: that the distri-

 0004-6256/88/030925-16$00.90

bution of velocities is a triaxial Gaussian, that the vertical distribution is isothermal, etc. One major goal of our study is to verify the conclusions of kinetic theories, to be able to test the assumptions that enter at each stage of the development.

A direct numerical simulation of a planetary ring is impossible, there are just too many particles. The compromise that has been used up to now is to limit the number of particles to a manageable number, say 100–200, and increase their size so they will collide with one another at a sufficiently rapid rate (e.g., Brahic 1977; Brahic and Hénon 1977; Lukkari 1981; Salo 1987). This approach can only provide a crude qualitative check on the analytic theories, though the experiments of Brahic did elucidate the importance of the finite size of the particles in the determination of the equilibrium velocity dispersion. The optical depths in these experiments are extremely low. Consequently, such experiments cannot be used to test detailed predictions of kinetic theories at realistic optical depths of order unity.

In this paper, we introduce a novel numerical method for studying the equilibrium properties of planetary rings. It is physically clear that the dynamics of the ring particles in one region of the ring are statistically completely independent of the dynamics of particles in other regions even a relatively short distance away. We can incorporate this intuition into our numerical model by only simulating a small region of the ring and representing more distant parts of the ring as copies of the simulated region. This is accomplished through an appropriate choice of periodic shearing boundary conditions. The unit cell must be large enough that there are no significant correlations between the motions of particles on opposite sides of the cell. Physically, we might expect that correlations would not be significant beyond a few particle radii. It is confirmed in our simulations that the two-particle correlation function is negligible beyond a couple of particle radii. Another important length scale is the radial mean free path, since, roughly speaking, viscosity arises because in a shearing situation the mean momentum of one region is carried over a distance comparable to the mean free path to be mixed with other regions where the mean momentum is different. The unit cell should also be larger than the mean free path. In all cases considered in this paper the mean free path is never more than a few particle radii, and typically much smaller. Thus the equilibrium properties of a planetary ring model can be well represented by the behavior of a patch of the ring only a few particles in extent. A closely analogous situation exists in the theory of liquids, where molecular dynamics experiments typically employ unit cells that are only a few molecular diameters in size (see Evans and Morriss 1984 for a review). Our work is most closely related to numerical studies of shearing granular flows such as occur in avalanches, grain elevators, etc. (Campbell and Brennan 1985; Campbell 1986).

The details of our numerical model are discussed in Sec. II. Included in this section are results that show the independence of the computed equilibrium properties and the size of the unit cell. We have verified that the $\epsilon(\tau)$ relation of Goldreich and Tremaine (1978) correctly gives the stability boundary for rings when the coefficient of restitution is independent of impact velocity. Equilibrium properties for three different ring models are presented in Sec. III, along with a comparison with the predictions of kinetic theories, where possible. Over the expected range of applicability, the kinetic theories are verified to be quite accurate. In particular, the conclusion of Araki and Tremaine (1986) that the $\tau\bar{\nu}$ condition for the viscous instability is not satisfied is confirmed, at least for all of the particular models investigated. The inclusion of the mean self-gravity has a dramatic effect on the equilibrium properties of the ring. The most surprising result is that at even moderate optical depths ($\tau \gtrsim 1$) the ring particles form horizontal layers or sheets. We present a summary of our results and conclusions in Sec. IV.

II. THE MODEL

a) Equations of Motion

Our model follows the dynamics of a collection of interacting particles, moving in the gravitational field of a planet. We assume that the system is azimuthally symmetric, and focus our attention on a small region located a radial distance r from the planet. The coordinates of particles in this region are referred to a reference point that moves on a circular orbit with semimajor axis a near r at the Keplerian angular velocity. We erect a rotating Cartesian coordinate sytem with origin at the reference position, the x axis pointing radially outward, the y axis pointing in the direction of the orbital motion, and the z axis normal to the equatorial plane.

If $x, y, z \ll r$, Newton's equations for the motion of the particles relative to the point of reference may be linearized (Hill 1978; Julian and Toomre 1966)

$$\begin{aligned} \ddot{x} - 2\Omega\dot{y} - 3\Omega^2 x &= -\frac{\partial\phi_p}{\partial x}, \\ \ddot{y} + 2\Omega\dot{x} &= -\frac{\partial\phi_p}{\partial y}, \\ \ddot{z} + \Omega^2 z &= -\frac{\partial\phi_p}{\partial z}, \end{aligned} \tag{1}$$

where $-\nabla\phi_p$ is the force per unit mass due to the other ring particles, and $\Omega = \sqrt{GM/a^3}$ is the mean motion of the reference position.

The solution of Eqs. (1) when $\phi_p \neq 0$ is

$$\begin{aligned} x &= x_0 + A\cos(\Omega t) + B\sin(\Omega t), \\ y &= y_0 - \tfrac{3}{2}\Omega x_0 t - 2A\sin(\Omega t) + 2B\cos(\Omega t), \\ z &= C\cos(\Omega t) + D\sin(\Omega t), \end{aligned} \tag{2}$$

where x_0, y_0, A, B, C, and D are constants of integration. The solution may be interpreted as having two contributions: the guiding center motion and the epicyclic motion. The guiding center motion represents the mean motion relative to the reference point. The epicyclic terms take into account the first-order effects of the orbital eccentricity.

Equations (2) have the constant of motion

$$H = \dot{y} + 2\Omega x = \dot{y}_r + \tfrac{1}{2}\Omega x, \tag{3}$$

where $\dot{y}_r \equiv \dot{y} + \frac{3}{2}\Omega x$ is the y velocity relative to the mean shear velocity at x. We shall call H the angular momentum, which is only a slight abuse of convention since the true angular momentum per unit mass in an inertial frame, $Ha + \Omega a^2$, differs from H only by additive and multiplicative constants.

b) Boundary Conditions

In order to restrict attention to a small patch, it is necessary to specify the behavior of the particles at the boundaries

of the patch. A property of the linearized equations (1) suggests an appropriate choice of the boundary conditions. The linearized equations are invariant under the transformation $x \to x + L_x$, $y \to y + L_y$, $\dot{x} \to \dot{x}$, $\dot{y} \to \dot{y} - \frac{3}{2}\Omega L_x$, where L_x and L_y are arbitrary. In other words, the dynamics of the linearized model are independent of the choice of origin, except for a uniform shear that is a consequence of the differential rotation in a Keplerian disk. If we make the plausible assumption that the dynamics of different portions of the ring are independent so long as they are sufficiently well separated, we can tile the ring plane with patches that are copies of one another. Thus, we assume that every particle has an infinity of image particles spaced at periodic intervals. A particle at (x, y, z) has images at $(x + nL_x, y - \frac{3}{2}nL_x\Omega t + mL_y, z)$, where n and m are integers, and L_x and L_y are arbitrarily chosen constants (which we generally take to be a few particle radii). The unit cell thus has a rectangular cross section with area $L_x \times L_y$, and infinite extent in the z direction. Whenever a particle center leaves the unit cell, one of its images enters the cell somewhere on the opposite face. In all the simulations reported here, we have taken the unit cell to be square, $L_x = L_y \equiv L$, except for some initial tests to verify that the equilibrium properties were independent of cell shape. These "sliding brick" unit cells were first used in studies of the transport properties of dense gases (Lees and Edwards 1972; Evans and Morriss 1984).

It is important to stress that the boundaries of the cell play no special role and that the model is independent of the location chosen for the unit cell. Exactly the same sequence of collisions would be obtained if the region called the unit cell was translated by an arbitrary horizontal displacement.

c) Constants of Motion

Let $u = \Sigma_{i=1}^{N} \dot{x}_i/N$, $w = \Sigma_{i=1}^{N} (\dot{y}_i + \frac{3}{2}\Omega x_i)/N$, where the sum is over all the particles in the unit cell. Notice that u and w are unchanged when particles cross the boundaries of the unit cell. The velocities u and w have many similarities to the center-of-mass velocity of a system of particles (notice that we use w rather than the true center-of-mass y velocity $v = \Sigma \dot{y}_i$ because v suffers a discontinuous jump when a particle crosses the edge of the unit cell). From equations (1), we have

$$\dot{u} - 2\Omega w = \sum_{i=1}^{N} \sum_{j=1}^{N} \mathbf{F}_{ij} \cdot \hat{x},$$

$$\dot{w} + \frac{1}{2}\Omega u = \sum_{i=1}^{N} \sum_{j=1}^{N} \mathbf{F}_{ij} \cdot \hat{y}, \tag{4}$$

where $\mathbf{F}_{ij}$ is the force per unit mass on particle i due to particle j. (In some cases, the particle will be interacting with an image particle outside the unit cell, but this does not affect the argument.) By Newton's third law, the terms on the right-hand side are zero and hence we may solve equations (4):

$$u = Ae^{i\Omega t} + Be^{-i\Omega t}; \quad w = \tfrac{1}{2}iAe^{i\Omega t} - \tfrac{1}{2}iBe^{-i\Omega t}, \tag{5}$$

where A and B are complex constants.

A particularly simple case occurs when the initial conditions are chosen such that the "center-of-mass" velocities u and w both vanish at the initial time $t = 0$. Then $A = B = 0$ and both the average radial velocity u and the average tangential velocity relative to the shear w are always zero. Moreover, we suffer no loss of generality if we consider only this case. To see this, let u_0 and w_0 be the values of u and w at $t = 0$. Then consider the transformation

$$x' = x + \frac{2w_0}{\Omega}\cos\Omega t - \frac{u_0}{\Omega}\sin\Omega t - \frac{2w_0}{\Omega},$$

$$y' = y - \frac{2u_0}{\Omega}\cos\Omega t - \frac{4w_0}{\Omega}\sin\Omega t + 3w_0 t + \frac{2u_0}{\Omega}. \tag{6}$$

The interparticle forces are unchanged by this transformation since the relative coordinates of two particles are unaffected. It is straightforward to show that x' and y' satisfy equations (1) and have $u' = w' = 0$. By using this transformation, the evolution of any unprimed system with $u \neq 0$, $w \neq 0$ can be determined from the evolution of the primed system with $u = w = 0$.

In the light of these results, from now on we shall consider only systems in which the "center-of-mass" motion $u = w = 0$. We have used the conservation of these quantities as a check on our numerical procedure; at the end of our simulations $|u/(\Omega L)|$ and $|w/(\Omega L)|$ are typically $\lesssim 10^{-12}$.

There are other constants of motion besides u and w. The angular momentum H (Eq. (3)) of each particle is conserved along its trajectory. Moreover, the total angular momentum of two particles is conserved during a collision (write $H_1 + H_2 = (\dot{y}_1 + \dot{y}_2) + 2\Omega(x_1 + x_2)$; since the collision is instantaneous, x_1 and x_2 do not change, and since the total momentum is conserved, $\dot{y}_1 + \dot{y}_2$ does not change). Thus the only change in the total angular momentum of the particles in the unit cell occurs from particles that enter or leave the cell. When a particle leaves across a face normal to $\hat{x}$ with positive x velocity, it is replaced by a particle whose angular momentum is smaller by $\frac{1}{2}\Omega L$. However, the average number of particles crossing this face in an interval Δt is $Nu\Delta t/L$; thus in a system with $u = 0$ at all times the time-averaged total angular momentum of the particles in the unit cell is constant.

Another constant of motion is $\Sigma_{i=1}^{N} \zeta_i$, where

$$\zeta = (\dot{x} + 2i\dot{y}_r)e^{i\Omega t}. \tag{7}$$

However, this constant will not be used or discussed in the remainder of this paper.

d) Interparticle Forces

In this first application of our method, we concentrate on the "standard" ring model, in which the particles are taken to be smooth inelastic hard spheres, all of the same radius R, and in which the detailed gravitational interactions between particles are ignored. Thus, a collision between two particles has negligible duration, and changes the radial and tangential relative-velocity components $v_\perp$ and $v_\parallel$ to

$$v_\perp' = -\epsilon v_\perp; \quad v_\parallel' = v_\parallel, \tag{8}$$

where ϵ is the coefficient of restitution (see, for example, Goldreich and Tremaine 1978). The tangential velocity is unchanged because the particles are taken to be smooth, i.e., there is no surface friction. Thus the particle spins are decoupled from the particle's translational motion. This assumption is made mainly so that our results can be compared with theoretical analyses; the inclusion of surface friction in the numerical model would be quite easy.

The neglect of gravitational interactions simplifies both theoretical and numerical calculations, at the cost of discarding an important effect. Gravitational scattering provides an efficient mechanism for converting relative orbital

motion into random motion, particularly when there is a distribution of particle sizes.

An additional effect of self-gravity is that the vertical gravitational field of the ring material increases the vertical frequency and compresses the ring, thereby enhancing the collision rate. This effect has been modeled crudely by modifying the third of equations (1) to read

$$\ddot{z} + \Omega_z^2 z = -\frac{\partial \phi_p}{\partial z}, \tag{9}$$

where

$$\Omega_z^2 = \Omega^2 + 4\pi G\rho \equiv g^2\Omega^2, \tag{10}$$

and ρ is the mean density in the midplane of the ring. Equation (9) is only approximate because it assumes that the density of ring material is uniform in z.

Until effects such as self-gravity, particle spin, and the particle-size distribution are included, our model cannot provide a realistic simulation of a planetary ring; however, it provides an important check on the analytic kinetic theories and it is appropriate to understand the behavior of this simplified model before adding extra complications.

e) Optical Depth

As is customary in studies of the dynamical behavior of planetary rings, we define the dynamical optical depth τ to be the sum of the projected areas of all the ring particles on the equatorial plane, divided by the projected area of the region they occupy. Note that τ is not equivalent to the physical optical depth τ_*, defined such that $\exp(-\tau_*)$ is the probability that a randomly chosen skewer $(x, y) = constant$ will not intercept a particle (although $\tau \approx \tau_*$ when $\tau \ll 1$, see Fig. 25). The dynamical optical depth τ is a fundamental parameter of the simulation; the physical optical depth τ_* is a derived property that takes into account the fact that some particles are obscured by other particles.

The number of particles whose centers lie in the unit cell is exactly constant in time and is denoted by N. In this study all particles have the same radius R. Thus the dynamical optical depth is

$$\tau \equiv \frac{N\pi R^2}{L_x L_y}, \tag{11}$$

where $L_x \times L_y$ is the projected area of the unit cell.

f) Numerical Methods

Since the trajectories of the ring particles are given by the explicit analytic expressions (2), the trajectory of a particle is completely specified by the epicyclic parameters A, B, C, D, x_0, and y_0. A list of the epicyclic parameters of all the particles completely specifies the state of the system and its time evolution from one collision to the next; the simulation proceeds directly from collision to collision. Thus, the primary task in the numerical simulation is the determination of whether a collision between two particles will occur and, if so, at precisely what time.

Within a particular time interval under consideration, collisions between two particles are first searched for by quadratic extrapolation of the distance between the particles as a function of time. The positions and velocities of the particles at the beginning of the interval are directly given by the epicyclic parameters; the accelerations are given by the equations of motion. If the quadratic extrapolation indicates that a collision occurs within the interval under consideration, the precise time of collision is found through repeated quadratic extrapolation in a manner analogous to the repeated linear extrapolations of Newton's method. If a collision is not detected, then it is still possible that a grazing collision occurred, and that the quadratic extrapolation was not adequate to detect it. To check for this possibility, the quadratic extrapolation is checked for a minimum within the interval. If a minimum is found, then the precise time of closest encounter is found, again by repeated quadratic extrapolation, this time to successive minima. If a grazing collision is detected, then the time of collision is found as before. In our simulation, the distance between two particles is a continuous function, but there are discontinuities in the time derivative. The discontinuity arises when the two particles move far enough away from each other that different images of these particles become closer together than the original two particles. To account for the possibility that a discontinuity may have occurred during the time interval under consideration, collisions are also searched for by quadratic extrapolation from the end of the interval backwards in time.

A "potential collision list" is used to manage the time evolution of the system and the actual execution of the collisions. Initially, all pairs of particles are examined to determine whether a collision will occur within a time Δt, which is of the order of the estimated mean time between collisions. A time-ordered list of the potential collisions is formed. Collisions at the head of this list are then executed successively; the epicyclic-state parameters for the two particles involved in the collision are replaced by post-collision epicyclic parameters. After each collision is executed, all entries in the collision list involving either of the two colliding particles are removed, and all pairs of particles involving either of the colliding particles are re-examined for impending collision. All potential collisions are appropriately added to the time-ordered collision list. In each case the time interval examined for collision is of length Δt. Since this time interval is finite, it may happen that the system evolves to a time beyond which a particular pair has been examined for collision. Thus it is necessary to keep a record of the time beyond which the fate of each pair is unknown; when these times are reached the appropriate pair must be re-examined. Collisions are only executed when all particles have been consistently advanced to the collision time. Likewise, statistics (such as the vertical histogram or filling factor) are only collected when the system has been consistently evolved to the time at which statistics are to be collected.

For a simulation involving N particles, the computer time required to update the collision list following a collision is proportional to N since the possibility of collision with all other particles must be re-examined, whereas the time required to initially construct the collision list is proportional to N^2, since all pairs must be examined. The time spent in re-examining those particles for which the interval Δt has expired is also proportional to N^2 in the limit where the time examined is very short, since all pairs will be continually in need of re-examination. It is thus advantageous to have this interval as long as possible. On the other hand, if Δt is too long, many potential collisions will have been found that will never occur and the computer time spent in finding them will have been wasted. Thus Δt should be of the order of the mean time between collisions.

g) Sliding Phase

The dynamics of two colliding smooth inelastic particles is surprisingly complicated in our model. It is possible for two particles to collide and then rebound with velocities that lead to recollision in a time much shorter than an orbit period. A sequence of such collisions is possible that completely damps the component of relative velocity perpendicular to the radius vector joining the particles. The two particles come to rest on each other and then slide around one another. This process has been discussed by Petit and Hénon (1986), who gave an analytic approximation for the motion during the sliding phase. The sliding phase requires special consideration in our simulation since an infinity of collisions occurs in a finite time, and we are solving the system exactly, stepping from collision to collision. It would be difficult to use an analytic approximation for the sliding phase in our simulation since other particles may collide with the particles undergoing the sliding motion. Instead, we have allowed for the sliding phase by providing a "cushion." The collisions are taken to be perfectly elastic once the relative radial velocities become less than a critical value. The subsequent motion is a sequence of small hops that effectively allow the particles to slide past one another. Without viewing the motion under a microscope, it is essentially the same as the sliding motion. We have taken this critical velocity to be $0.01\Omega R$, which is typically less than 1% of the random velocities.

h) Initial Conditions

The initial x and y coordinates of the particles are chosen at random, uniformly distributed across the unit cell. The vertical distribution is also taken to be uniform up to a distance h above and below the equatorial plane. This initial boxlike distribution is clearly not near equilibrium and was chosen to avoid the possibility that any particular equilibrium was chosen by accident. The initial velocities are also randomly chosen with a uniform distribution up to a given maximum velocity in each of the Cartesian components (arbitrarily taken to be ΩR), which is slightly lower than the equilibrium random velocities). The positions of pairs of particles are chosen symmetrically so that the center of mass will be at the center of the unit cell; the velocities are chosen independently, except for the last particle, which is given a velocity so that the total momentum in the cell is zero. We shall argue below that the ring rapidly reaches an equilibrium state that is independent of the initial conditions.

i) Angular-Momentum Transport

One of the most important properties of a differentially rotating disk is the rate of radial angular-momentum transport, which is closely related to the viscosity.

From a microscopic viewpoint, there are two distinct contributions to the angular-momentum transport. The first arises from momentum carried across a surface by the physical motion of a particle actually crossing the surface. This will be referred to as "local" transport (also sometimes called "translational," "kinetic," or "streaming" transport), since it is present even in a fluid of point particles in which interparticle forces have zero range. The second arises when two particles undergo a collision that straddles the surface under consideration. This mechanism will be referred to as "nonlocal" transport (also called "collisional" or "potential" transport). In this case, the local transport of momentum across the surface is through sound waves in the particles themselves. Since in our model the particles only interact through hard-sphere collisions that are instantaneous, there is no ambiguity about the moment of collision or the separation of the local and nonlocal contributions to the angular-momentum transport.

It would be highly inefficient to compute the rates of these two transport mechanisms by considering the momentum flux across a particular surface in the simulation. We have emphasized above that all points in the unit cell are dynamically equivalent. A more computationally efficient estimate of the transport coefficients can be made by taking the average of the transport rates across a large number of surfaces in the unit cell. It is a small step then to consider an infinity of such surfaces, which implies that the most efficient estimates of the transport rate are based on a time average over the particle trajectories.

Let the angular-momentum flux Φ be the outward flow rate of angular momentum per unit length; thus ΦL is the rate of flow of H (Eq. (3)) across the surface S defined by $x = x_0$, $y_0 \leqslant y_0 + L$, where x_0 and y_0 are arbitrary and the flow is positive in the direction from $x < x_0$ to $x > x_0$. The local flux Φ_L arises from particles whose centers cross S. We may write

$$\Phi_L L dt = \sum_{\text{out}} (\dot{y}_{ri} + \tfrac{1}{2}\Omega x_0) - \sum_{\text{in}} (\dot{y}_{ri} + \tfrac{1}{2}\Omega x_0), \tag{12}$$

where "out" denotes a sum over all particles i that cross S with $\dot{x}_i > 0$, while "in" denotes a sum over particles that cross with $\dot{x}_i < 0$. The location of the surface S is arbitrary and hence the probability that any particle i will cross S during dt is $|\dot{x}_i| dt/L$. Hence we may rewrite Eq. (12) as

$$\Phi_L = \frac{\Sigma_{i=1}^{N} \dot{x}_i \dot{y}_{ri}}{L^2} + \frac{\Omega x_0}{2L^2} \sum_{i=1}^{N} \dot{x}_i. \tag{13}$$

The second term in Eq. (13) is proportional to the mean radial speed u. We have shown that we can restrict ourselves to the case $u = 0$ without loss of generality, and hence this term will be dropped from now on.

The nonlocal flux Φ_{NL} arises from collisions between two particles whose centers are on opposite sides of the surface S. Each such collision transports across S an angular momentum $\Delta\dot{y}_>$ equal to the change in y velocity of the particle with $x > x_0$. The probability that the two centers in a given collision span S is $(x_> - x_<)/L$ and hence

$$\Phi_{NL} = \frac{\Sigma (x_> - x_<) \Delta \dot{y}_>}{L^2 dt}, \tag{14}$$

where the sum is over all collisions occurring during the interval dt.

j) Viscosity

For a fluid, the dynamic viscosity η is usually defined as the proportionality factor that relates the force per unit area to the shear rate:

$$\frac{F}{A} = \eta \frac{du_y}{dx}, \tag{15}$$

where u_y is the mean flow velocity of the fluid. For a planetary ring with nonuniform vertical structure, it is more useful to speak of the "height-integrated" dynamic viscosity $\bar{\eta}$

which is defined as the proportionality factor that relates the total force transmitted across a given radius per unit length to the shear rate:

$$\frac{F}{L} = \bar{\eta}\frac{du_y}{dx}. \tag{16}$$

In a Keplerian potential, $u_y = -\frac{3}{2}\Omega x + \text{const}$. The kinematic viscosity ν is related to the dynamic viscosity by $\eta = \rho\nu$, where ρ is the bulk fluid density. Analogously, for a planetary ring the "height-averaged" kinematic viscosity $\bar{\nu}$ is related to the height-integrated dynamic viscosity by $\bar{\eta} = \sigma\bar{\nu}$, where σ is the surface density. We shall refer to the height-averaged kinematic viscosity simply as the kinematic viscosity or even just the viscosity.

In a steady state, the angular-momentum flux Φ is simply related to the viscosity. Since the mean radial speed is zero in the steady state, the rate of flow of angular momentum per unit mass across a surface of length L, ΦL, is equal to F/m, where F is given by Eq. (16) and m is the particle mass. Taking proper account of signs, we find

$$\bar{\eta} = \frac{2m\Phi}{3\Omega}; \quad \bar{\nu} = \frac{2m\Phi}{3\Omega\sigma}. \tag{17}$$

The surface density can be written in the form $\sigma = Nm/(L_x L_y)$, and with the use of Eq. (11) for the dynamical optical depth τ we have

$$\bar{\nu} = \frac{2\pi R^2}{3\Omega\tau}\Phi. \tag{18}$$

We can define local and nonlocal contributions to the viscosity by replacing Φ by Φ_L and Φ_{NL}. From Eq. (13) the local height-averaged kinematic viscosity is

$$\bar{\nu}_L = \frac{2}{3\Omega}\langle \dot{x}\dot{y}_r \rangle_{p,t}, \tag{19}$$

where $\langle\cdot\rangle_p$ and $\langle\cdot\rangle_t$ denote averages over the particles in the unit cell and over time. The nonlocal viscosity is

$$\bar{\nu}_{NL} = \frac{2}{3\Omega}\frac{1}{NT}\sum (x_> - x_<)\Delta\dot{y}_>, \tag{20}$$

where the sum is over all collisions occurring during the time interval T.

k) Velocity Ellipsoid

The orientation and magnitude of the principal axes of the velocity-dispersion tensor define the velocity ellipsoid. The components of the velocity-dispersion tensor are computed as time averages over products of particular components of the velocity dispersion, averaged over all the particles. Since the analytic expressions for the particle trajectories are simple, the time averages for each particle are computed analytically from one collision to the next. Each contribution to the average depends only on the epicyclic parameters and the times at which the trajectory segment begins and ends. For example, the contribution to the xy component of the velocity-dispersion tensor from particle p between collisions at t_1 and t_2 is

$$\frac{\Omega}{8(t_2 - t_1)}\{(B_p^2 - A_p^2)[\cos(2\Omega t_2) - \cos(2\Omega t_1)] - 2A_pB_p[\sin(2\Omega t_2) - \sin(2\Omega t_1)]\}.$$

l) Vertical Distribution, Filling Factor, and Optical Depth

Several quantities are estimated by sampling the simulation many times per orbit, typically one hundred. These quantities include the vertical distribution function, the filling factor, and the physical optical depth τ_*. The sampling begins after examination of the velocity dispersions indicates that equilibrium has been reached, and extends to the end of the run. The vertical distribution is determined by binning $|z|$ of all particles at the sampling times. The filling factor at the midplane ($z = 0$) is computed as the average fraction of the area of the midplane of the unit cell that is inside any particle. The physical optical depth is computed by shooting one hundred skewers on a square lattice vertically through the simulation at each sampling time. The physical optical depth is defined so that $\exp(-\tau_*)$ is the average fraction of skewers that penetrate the ring without piercing any particles.

m) Number of Particles

We have found that reliable results can be obtained from simulations with small numbers of particles. For example, Fig. 1 shows the principal axes of the velocity ellipsoid as a function of the number of particles N (the parameters for this run, in the notation of the following section, are $\tau = 1$ and case (i)). Each of these runs lasted 20 orbital periods, and the error bars, which represent the standard deviation of the mean, are determined by treating the average over each orbital period as an independent measurement. There is very little systematic trend in the results with N for $N > 0$ in this or any other quantity that we analyzed. Hence it should be possible to obtain accurate results with N as small as 20, although we typically used a larger and more conservative value, $N = 40$. In general, we expect that simulations of this kind should be reliable so long as N is sufficiently large that the cell size L exceeds both the mean free path and the particle size. For example, for optical depth $\tau = 1$, particle radius

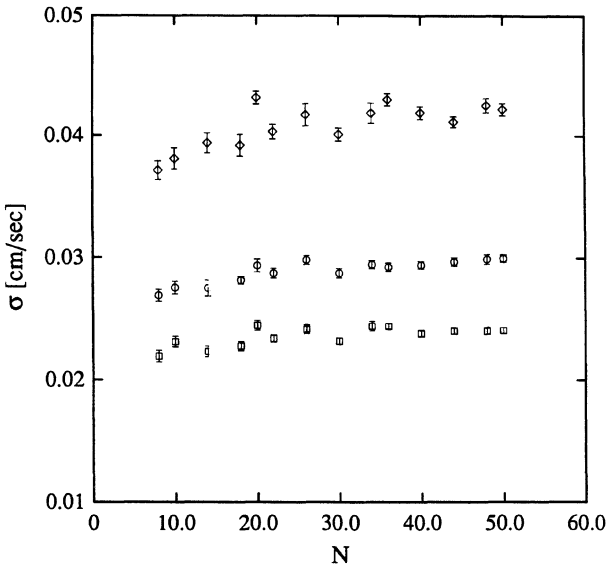

FIG. 1. Principal axes of the velocity ellipsoid as a function of the number of particles N, for model (i) with optical depth $\tau = 1$. In general, the middle-size axis of the velocity ellipsoid is the z axis.

R, and $N = 20$, a square unit cell has sides of length $L = \sqrt{N\pi R^2/\tau} \simeq 7.9R$, which is a healthy margin larger than both the particle size and the mean free path, which for these parameters is of order R.

n) Establishment of Equilibrium

Goldreich and Tremaine (1978, hereafter referred to as GT) emphasized that a velocity-dependent coefficient of restitution was essential to establish equilibrium in a dilute ring. The reason is that in a dilute ring the rate of increase of random energy due to viscous dissipation is proportional to the square of the velocity dispersion, σ^2, while the rate of decrease of random energy due to inelastic collisions is proportional to $(1-\epsilon^2)\sigma^2$. If the coefficient of restitution is independent of velocity, these two rates are generally unequal, no matter what the dispersion may be. Hence the ring either explodes, or collapses to a monolayer. On the other hand, a velocity-dependent coefficient of restitution permits the ring to establish a velocity dispersion at which the energy-input rate balances the energy-dissipation rate.

The $\epsilon(\tau)$ relation defines the unique coefficient of restitution at which equilibrium is attained for a given optical depth. If the coefficient of restitution is independent of velocity, the $\epsilon(\tau)$ relation may be viewed as a stability boundary. For a given optical depth, if the coefficient of restitution is larger than given by the $\epsilon(\tau)$ relation, the ring thickness will exponentially increase; if the coefficient of restitution is smaller than that given by the $\epsilon(\tau)$ relation, the ring collapses to an approximate monolayer, in which the magnitude of the velocity dispersion is of the order of the shear across a particle diameter (Brahic 1977). We have verified that the $\epsilon(\tau)$ relation does indeed provide a stability boundary for our model, by investigating the stability of rings of optical depth $\tau = 1$, for velocity-independent coefficients of restitution equal to integral multiples of 0.1. The $\epsilon(\tau)$ relation of GT implies a stability boundary $\epsilon \simeq 0.82$. Up to $\epsilon = 0.8$, the numerical model reaches equilibrium, with the equilibrium velocity dispersion increasing with the coefficient of restitution. For $\epsilon = 0.9$, however, the velocity dispersions increase roughly exponentially with time, with an e-folding time of about three or four orbit periods. We made no attempt to further refine the stability boundary for the numerical model, but our results are completely consistent with the GT prediction.

Figure 2 shows the principal axes of the velocity-dispersion tensor as a function of time in a similar run but with $\tau = 0.4$. The particles were intially distributed uniformly in z, with a thickness of $10R$. The ring layer collapses to equilibrium over the first few orbit periods, as illustrated by the velocity dispersions in Fig. 2. For higher optical depths, the approach to equilibrium is more rapid. The simulation is considered to have reached "equilibrium" when the principal axes of the velocity ellipsoid appeared to have reached stationary values. In this case, equilibrium has apparently been reached after about seven or eight orbit periods. All estimates of equilibrium properties were based on time averages starting from that point at which the disk appeared to be in equilibrium, and lasting until the end of the run.

IV. EQUILIBRIUM PROPERTIES

We have run extensive simulations for three different models for the coefficient of restitution ϵ and the self-gravity enhancement factor g:

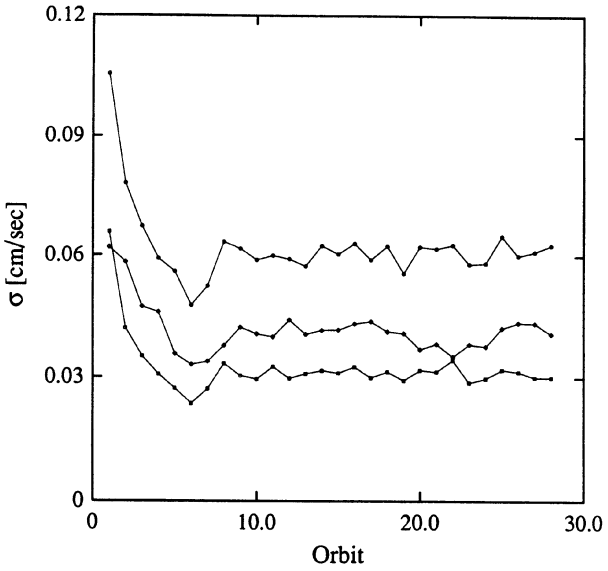

FIG. 2. Principal axes of the velocity ellipsoid as a function of time, for model (i) with $\tau = 0.4$. Equilibrium has apparently been established after seven or eight orbit periods. At higher optical depth, the approach to equilibrium is more rapid.

(i) velocity-dependent coefficient of restitution determined experimentally by Bridges *et al.* (1984), no self-gravity vertical frequency enhancement ($g = 1$), particle radius $R = 100$ cm, and angular speed $\Omega = 1.95 \times 10^{-4}$ radian s^{-1}, appropriate for the center of Saturn's B ring. Specifically, the Bridges–Hatzes–Lin coefficient of restitution is $\epsilon(v_\perp) = \min\,[0.34(v_\perp)^{-0.234}, 1]$, with v in cm s^{-1}.

(ii) velocity-independent coefficient of restitution $\epsilon = 0.5$, and no self-gravity vertical frequency enhancement ($g = 1$).

(iii) velocity-independent coefficient of restitution $\epsilon = 0.5$, and self-gravity vertical frequency enhancement $g = 3.6$ (roughly correct for the center of Saturn's B ring if $\rho = 0.4$ g cm^{-3}).

a) Comparison with Boltzmann Theory

We first compare results of our simulation with the analytical model of GT. The GT model is an approximate solution of the Boltzmann equation. The Boltzmann equation assumes that the phase-space distribution function is adequately represented by a product of single-particle distribution functions. The approximations used by GT to solve the Boltzmann equation include (1) the neglect of third-order velocity moments of the Boltzmann equation to close the system, (2) the assumption of a triaxial Gaussian velocity distribution to evaluate the collision integrals, (3) the neglect of the finite particle size, which limits applicability to small filling factors, and (4) the neglect of the self-gravity of the particles. Approximation (1) leads to an error of order $(v/\Omega r)$, where v is a typical random velocity; since this ratio is $\lesssim 10^{-6}$ in Saturn's rings the approximation is very good. Approximation (2) is unlikely to lead to substantial errors. Approximation (3) leads to no additional error since the Boltzmann equation is only valid for small filling factors in any case. Approximation (4) is also made in our numerical

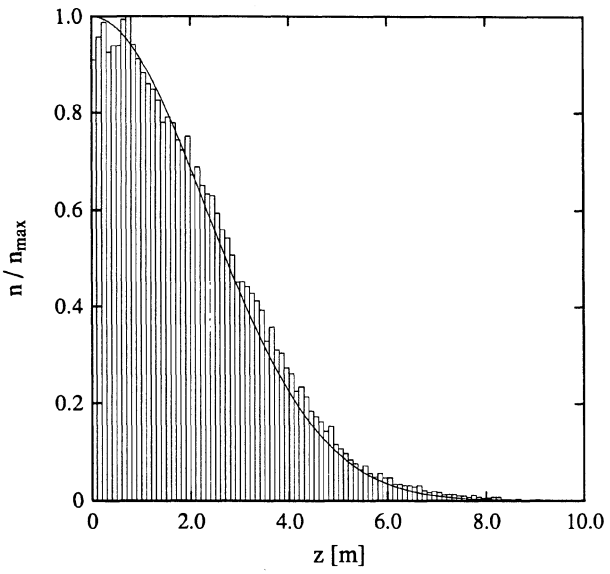

FIG. 3. Histogram of the particle number density as a function of distance from the midplane ($z = 0$), for model (i) with $\tau = 0.2$. The curve represents Eq. (21), with the velocity dispersion determined from the simulation. This is an excellent approximation at low optical depths.

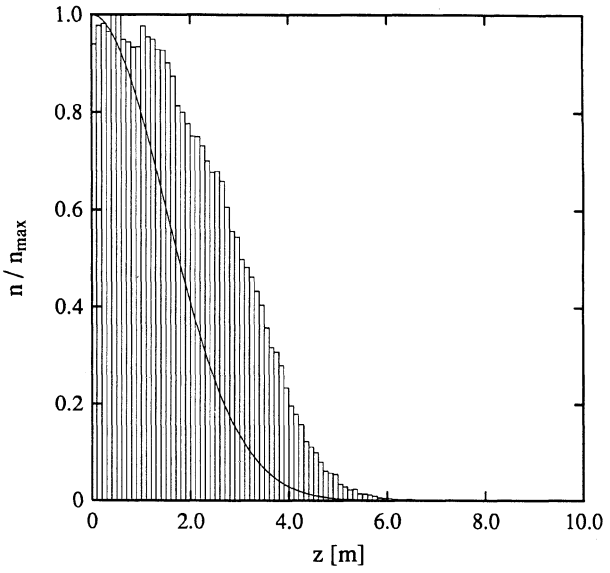

FIG. 4. Histogram of the particle number density as a function of distance from the midplane ($z = 0$), for model (i) with $\tau = 1.0$. Approximation (21) begins to break down as the particles pile up on one another and the filling factor is no longer negligible.

simulations and so does not affect the comparison of our results to the GT model.

An additional assumption made for convenience is that the velocity ellipsoid is independent of height above the ring plane. Then the vertical density distribution is

$$n(z) = n(0)\exp(-\tfrac{1}{2}\Omega_z^2 z^2/\sigma_3^2), \qquad (21)$$

where σ_3 is the principal axis of the velocity-dispersion tensor perpendicular to the orbit plane. Figure 3 illustrates that at low optical depths this is an excellent approximation for model (i). The curve represents Eq. (21) with the velocity dispersion $\sigma_3 = 0.0450 \pm 0.0007$ cm/s, determined from the simulation. The histogram is generated by sampling the height of all the particles one hundred times per orbit period after equilibrium has been reached and until the end of the run, which in this case lasted 30 orbit periods. The number of particles was 50. On the other hand, Fig. 4 illustrates that at optical depths as low as $\tau = 1$ the approximation (21) begins to break down as the particles pile up on one another; the filling factor is no longer negligible. Here the velocity dispersion was measured to be $\sigma_3 = 0.0292 \pm 0.0003$ cm s^{-1}.

Next we consider the horizontal dynamics. The predicted orientation of the velocity ellipsoid is compared to that observed in the simulation in Fig. 5. Here δ is the angle between the $\hat{x}$ axis and the nearest principal axis of the velocity ellipsoid. Surprisingly, there is excellent agreement at all optical depths, despite the failure of Eq. (21) for the vertical equilibrium. (The increased scatter of the numerical results for $\tau \geqslant 2$ is a result of using fewer particles (30) for fewer orbit periods (20) to save computer time.) The agreement with the predicted principal-axis ratios is, however, not as good. Figure 6 shows the comparison. Only the general trend is reproduced. For the ratio σ_2/σ_1 there is fair agreement at low optical depth where the GT model should be valid. We would say the same for the other ratio were it not for the one point at $\tau = 0.2$; it may, however, be that the disagreement here is just a statistical fluctuation, a conclusion consistent with an extrapolation by eye down the data points. The dimensionless height-averaged viscosity is shown in Fig. 7. GT only calculated the local contribution to the height-averaged viscosity; the line marks their prediction. The data points show both the local viscosity and the total (local plus nonlocal) viscosity. At low optical depths, where the GT model should apply, the local viscosity does indeed dominate the viscosity and the agreement is satisfactory. However, at higher τ the nonlocal contribution is much more important, and the GT prediction for the viscosity is clearly inadequate for $\tau \gtrsim 0.5$.

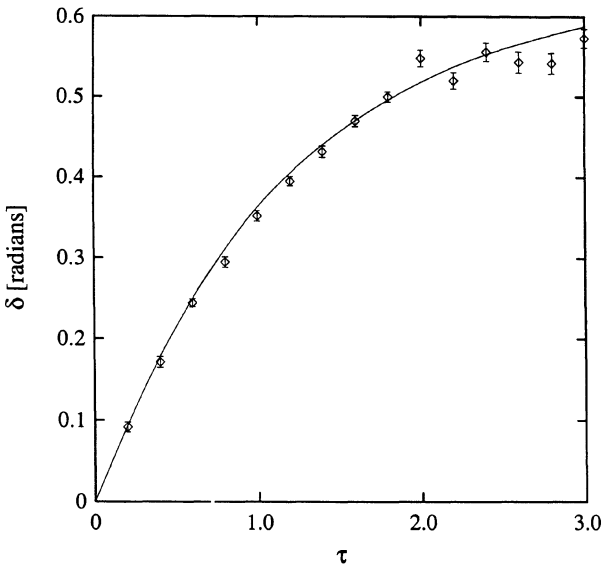

FIG. 5. Orientation of the velocity ellipsoid as a function of optical depth, for model (i). The line indicates the prediction of Goldreich and Tremaine (1978). The agreement is surprisingly good.

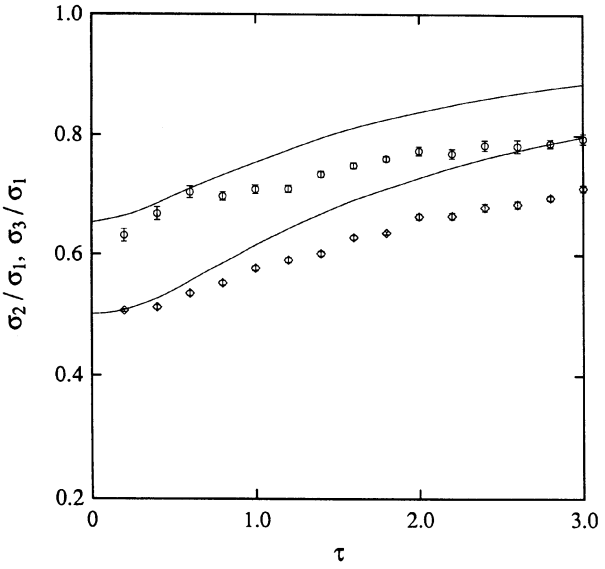

FIG. 6. Ratios of the principal axes of the velocity ellipsoid as a function of optical depth, for model (i). The line indicates the prediction of GT.

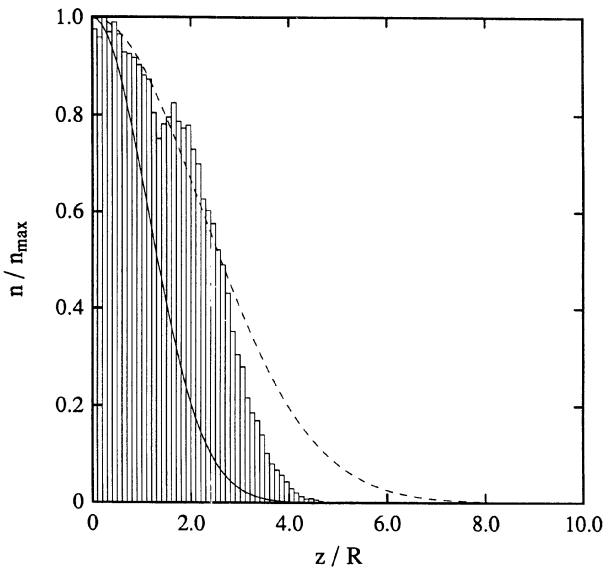

FIG. 8. Histogram of the particle number density as a function of distance from the midplane ($z = 0$), for model (ii) with $\tau = 1.0$. The Gaussian profile determined by the Araki and Tremaine (1986) model is shown as a dashed line; the solid line shows Eq. (21). The AT profile is not bad, considering that the Gaussian has been insisted upon.

b) Comparison with Enskog Theory

Araki and Tremaine (1986, hereafter referred to as AT) generalized the kinetic theory of GT to the case where the filling factor is not small by employing the Enskog theory of dense hard-sphere gases. The Enskog theory differs from the Boltzmann theory in the calculation of the collision integral. The Enskog theory includes the "nonlocal" transport of momentum across particles during collisions, and the enhancement of the collision frequency that occurs because the finite size of the particles reduces the free volume. In some of these calculations the vertical distribution is again taken to be a Gaussian for convenience, though Eq. (21) does not apply since the root-mean-square (rms) thickness is not directly proportional to the dispersion σ_3. Araki (1987) has provided calculations for model (ii), i.e., velocity-independent coefficient of restitution $\epsilon = 0.5$, with no self-gravity enhancement factor $g = 1$, for comparison with our simulations. In this case, the number of particles was 30 and each run was continued for 30 orbit periods. The vertical distributions are compared in Fig. 8. The dashed line is the Gaussian profile determined by the AT model; the solid line is the profile determined by Eq. (21) and the velocity dispersion determined from the simulation $\sigma_3 = 0.0218 \pm 0.0003$ cm s^{-1}. The AT profile is quite good, considering that it has been forced to be Gaussian. In Fig. 9 the vertical distributions for $\tau = 2$ are compared. The agreement with the AT profile is still quite good, considering that the Gaussian profile has been insisted upon. The profile predicted by Eq. (21) is sorely inadequate; here $\sigma_3 = 0.01926 \pm 0.0002$ cm s^{-1}. The AT prediction of the orientation of the velocity ellipsoid (Fig. 10) is in excellent agreement at low optical depths, and still satisfactory at higher τ. The ratios of the principal axes of the velocity ellipsoid predicted by the Enskog theory are in much better agreement with the results of the simulation than were the predictions of the GT model (Fig. 11). For reference, the magnitudes of the individual principal axes of the velocity ellipsoid are shown in Fig. 12, again with the AT predictions. The predictions clearly fall outside the estimated error of the simulation results; nevertheless, the qualitative agreement is quite satisfactory at all τ.

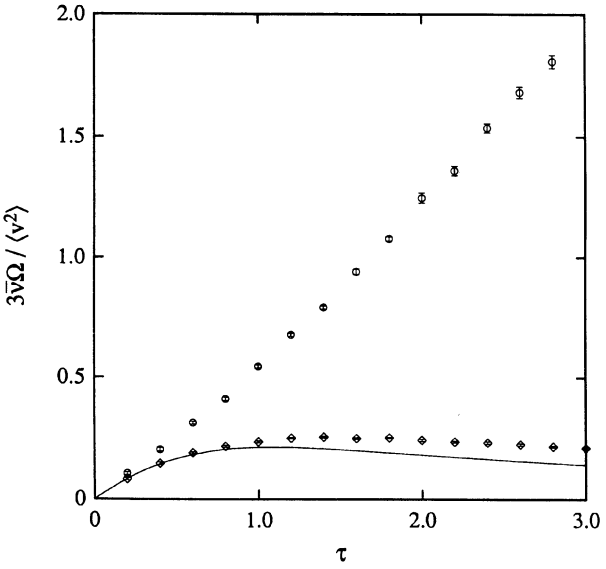

FIG. 7. Dimensionless height-averaged kinematic viscosity as a function of optical depth, for model (i). Both local viscosity (diamonds) and total (local plus nonlocal) viscosity (circles) are indicated. The line marks the prediction of GT. At high optical depths the nonlocal contribution dominates the viscosity.

c) Viscous Stability in Models without Self-Gravity

A principal conclusion of AT was that the $\tau\bar{\nu}$ condition for the viscous instability was not realized. Both components of

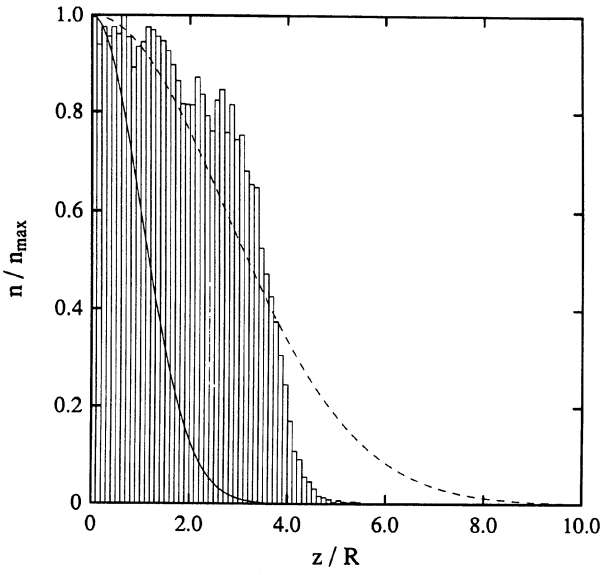

FIG. 9. Histogram of the particle number density as a function of distance from the midplane ($z = 0$), for model (ii) with $\tau = 2.0$. The Gaussian profile determined by the Araki and Tremaine (1986) model is shown as a dashed line; the solid line shows Eq. (21). The AT profile is still quite good, considering that the Gaussian has been insisted upon.

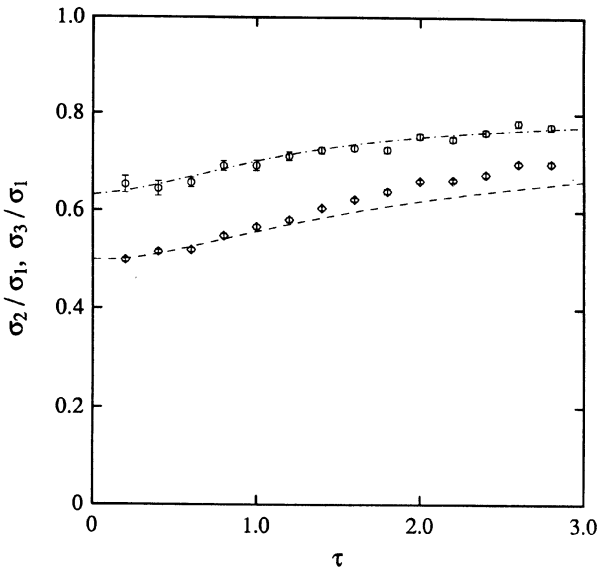

FIG. 11. Ratios of the principal axes of the velocity ellipsoid as a function of optical depth, for model (ii). The lines indicate the predictions of AT.

the viscosity are computed in the AT model. Figure 13 shows the comparison with the simulation. Again, the qualitative agreement is good. The condition for the viscous instability is that there be an interval in τ over which the product of the viscosity and the optical depth ($\tau\bar{\nu}$) have negative slope. The quantity $\tau\bar{\nu}$ is plotted versus τ in Fig. 14. The condition for the viscous instability is clearly not realized under the assumptions of our numerical model. The corresponding plot for model (i) with a velocity-dependent coefficient of restitution is very similar, and likewise does not give any indication for the viscous instability.

d) Filling Factor in Models without Self-Gravity

The computed filling factor or solid fraction at the midpoint of the ring plane, $FF(z = 0)$, for models (i) and (ii) is shown in Fig. 15, together with the prediction of the AT theory for model (ii). The filling factor for model (i) is lower than that for model (ii), especially at the larger τ. The filling factor where a nonshearing gas of elastic hard spheres undergoes a phase transition is near 0.48. For these two

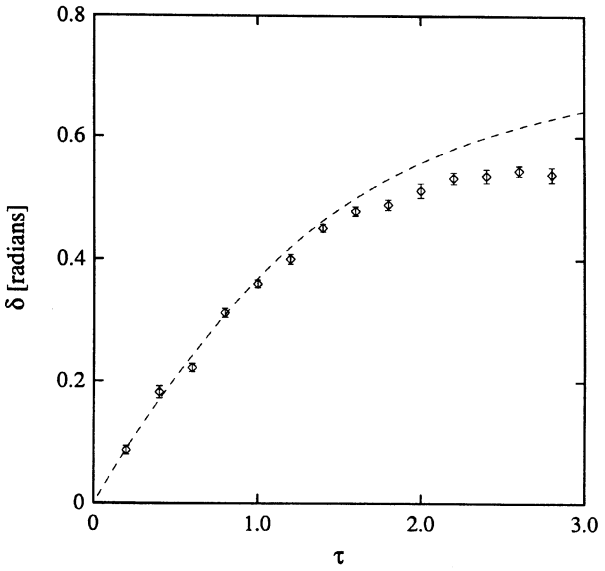

FIG. 10. Orientation of the velocity ellipsoid versus optical depth, for model (ii). The prediction of AT is indicated by a dashed line. The agreement is excellent at low optical depths, and still satisfactory at higher optical depths.

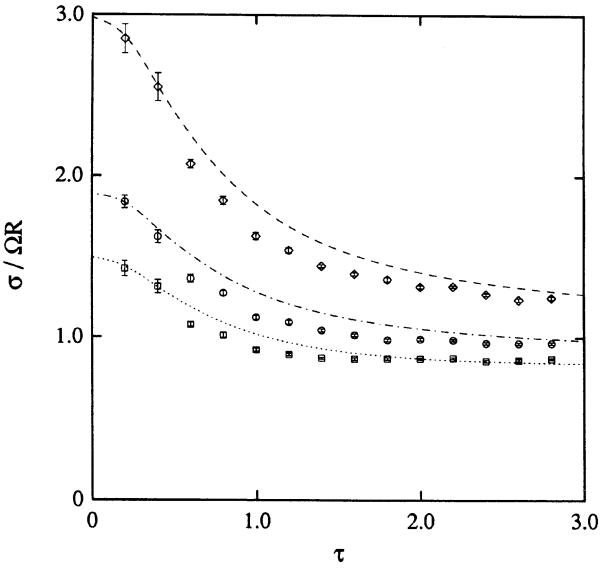

FIG. 12. Magnitudes of the principal axes of the velocity ellipsoid versus optical depth, together with the predictions of AT, for model (ii).

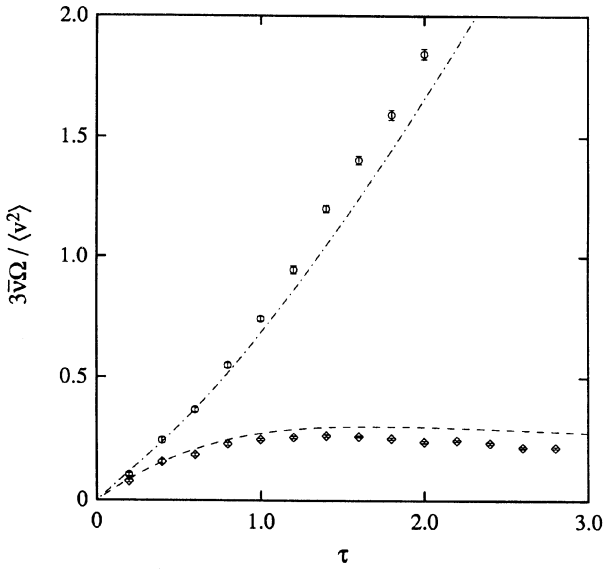

FIG. 13. Dimensionless height-averaged kinematic viscosity versus optical depth for model (ii). The local viscosity (diamonds) and total viscosity (circles) are compared to the predictions of AT. The qualitative agreement is quite good.

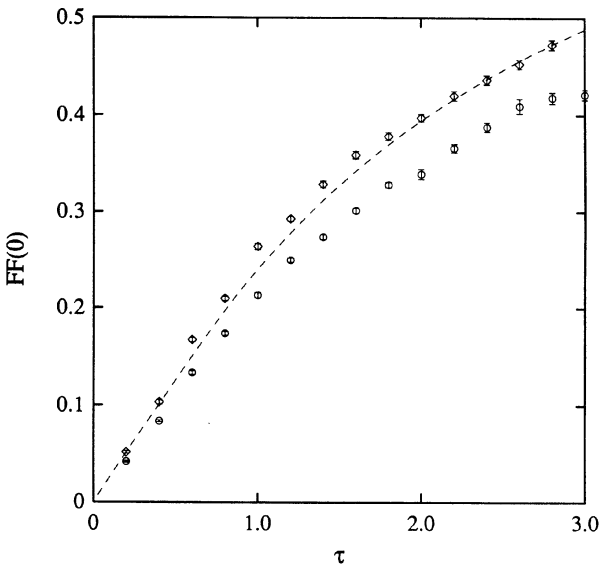

FIG. 15. The filling factor at the midplane ($z = 0$) versus optical depth, for models (i) (circles) and (ii) (diamonds). The line indicates the prediction of AT for model (ii).

models in which there is no self-gravity enhancement ($g = 1$), this filling factor is only reached for optical depths above 3. However, the computer time required to simulate rings with $\tau > 3$ is large, and simulations in this regime have not been undertaken, for the following reason. When average self-gravity is included, high filling factors are reached at much lower τ. Thus, making the model more realistic eases the computing requirements.

e) Self-Gravity Model

The average effect of the self-gravity of the particles has been modeled by a simple enhancement of the vertical restoring force (Eq. (9)). This is strictly valid only for a disk of uniform density. Thus, this simple model probably offers a good representation of the interior of the ring, but is less realistic for the vertical extremities. This simple enhancement of the restoring force preserves the harmonic-oscillator form of the vertical equations of motion. The solution remains a simple harmonic oscillation (but with an enhanced frequency), and the particle trajectories are still analytic. We have taken in model (iii) a self-gravity vertical frequency enhancement factor of $g = 3.6$, which is a physically plausible value for the middle of Saturn's B ring. The coefficient of restitution was taken to be independent of velocity with value $\epsilon = 0.5$ as in model (ii). In these simulations we took $N = 40$, and the simulations were run for 20 orbit periods.

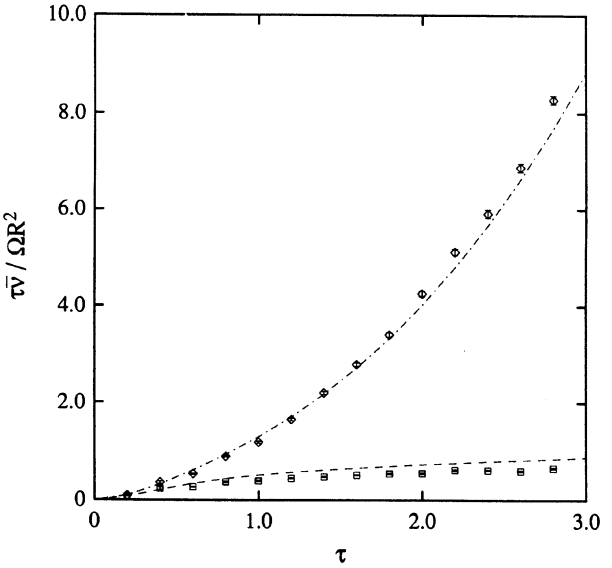

FIG. 14. The quantity $\bar{\tau\nu}$ versus optical depth, for model (ii). The curves represent local and total viscosity. The condition for the viscous instability, that the slope be negative over some interval of τ, is not satisfied.

The inclusion of self-gravity has a dramatic effect on the equilibrium properties of the simulated ring. This is most immediately noticed in the number of collisions per particle per orbit. Figure 16 shows the common logarithm of the number of collisions per particle per orbit for our three models. Particles in the self-gravity model suffer about two orders of magnitude more collisions per unit time than particles in the models without self-gravity. The collision frequency is very large compared to the orbital frequency.

The principal axes of the velocity ellipsoid are shown in Fig. 17. The magnitudes of the velocity dispersions are comparable to the velocity dispersions in the two other models. This reflects the fact that this velocity dispersion is maintained by the shearing of particles past one another. The typical shear velocity between two particles separated by two particle radii is $3\Omega R$; this determines the scale of the velocity dispersions. The components of the velocity dispersion are more nearly equal in this model than in the two other models; as a consequence of the high collision rate, the ring behaves more like a fluid in this model.

The concept of mean free path in our model is complicated by the curvature of the particle trajectories. For simplicity, we simply define the mean free path λ to be the product of the mean time between collisions and the rms velocity, i.e.,

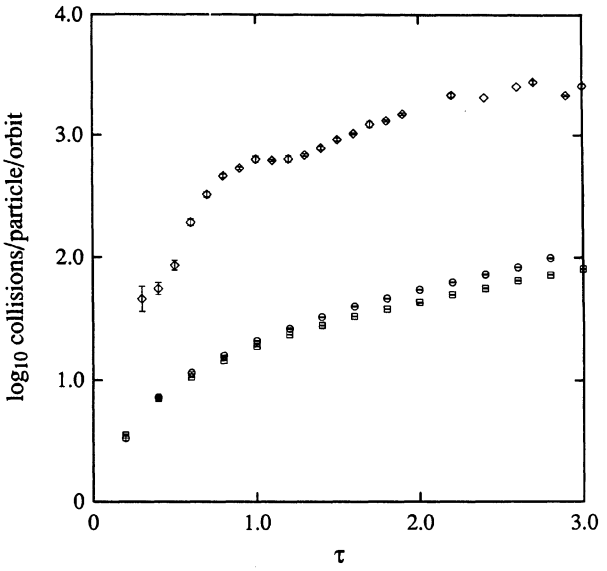

FIG. 16. The common logarithm of the number of collisions per particle per orbit for all three models (model (i)–squares, model (ii)—circles, model (iii)—diamonds), as a function of optical depth. Particles suffer about two orders of magnitude more collisions per unit time in the self-gravity model than in models without self-gravity.

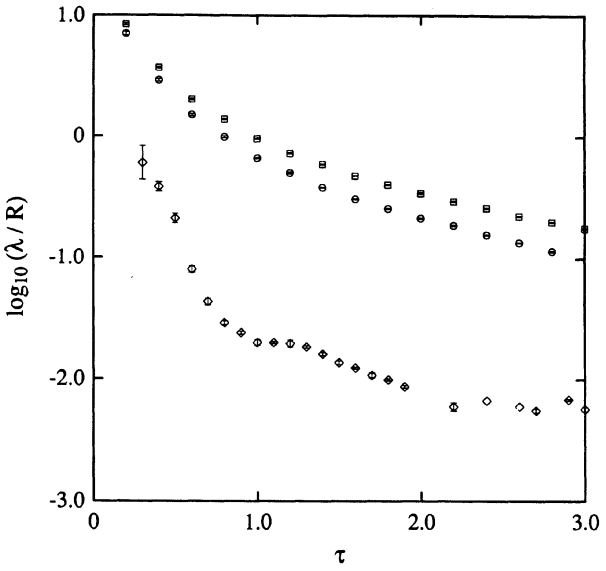

FIG. 18. Common logarithm of the mean free path versus optical depth for the three models (model (i)—squares, model (ii)—circles, model (iii)—diamonds). The mean free path is generally much smaller than the particle size in model (iii).

the square root of the sums of the squares of the principal axes of the velocity ellipsoid. The logarithm of the mean free path is shown in Fig. 18. This plot emphasizes that the mean free path is generally smaller than the particle size, and in the self-gravity model much smaller than the particle size.

Once again, there is no evidence for the viscous instability in the plot of $\tau\bar{\nu}$. Figure 19 shows a monotonic increase of $\tau\bar{\nu}$ with τ. The magnitude of the viscosity, which is almost entirely the nonlocal viscosity, is about a factor of 5 larger in the self-gravity model than in the other models.

The filling factor at the midplane $FF(z = 0)$ reaches large values at quite low optical depths. Figure 20 shows that $FF(0)$ undergoes an oscillation with optical depth. Already, by optical depth $\tau = 0.7$ the filling factor is above the value 0.48 at which a stationary hard-sphere gas undergoes a phase transition. For $\tau > 0.7$ the filling factor oscillates with τ. The first peak in $FF(0)$ occurs at $\tau = 0.9$ and has the value $FF(0) = 0.531$. The first minimum then occurs at $\tau = 1.3$ with magnitude $FF(0) = 0.486$. The next maximum occurs

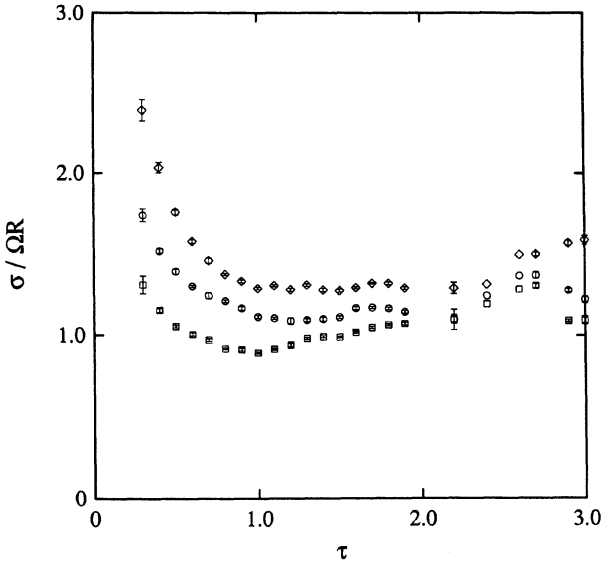

FIG. 17. Principal axes of the velocity ellipsoid versus optical depth for the self-gravity model (iii). The velocity dispersions are more nearly equal in this model than in the other models; as a consequence of the high collision rate, the ring behaves more like a fluid in this model.

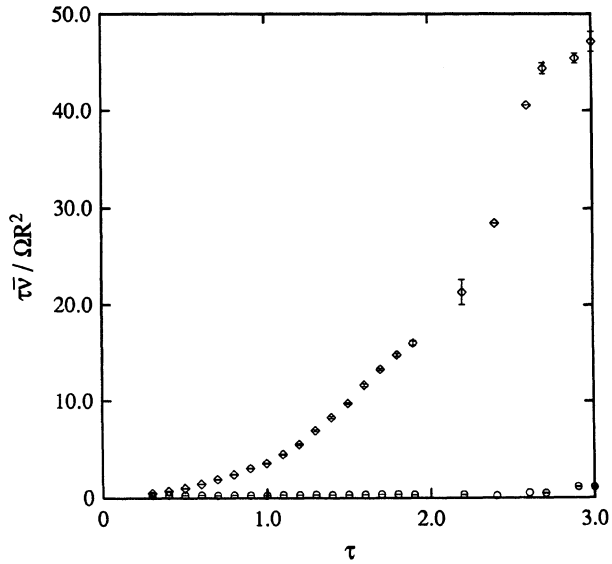

FIG. 19. The quantity $\tau\bar{\nu}$ versus optical depth, for the self-gravity model (iii). The curves represent local and total viscosity. The $\tau\bar{\nu}$ condition for the viscous instability is not satisfied.

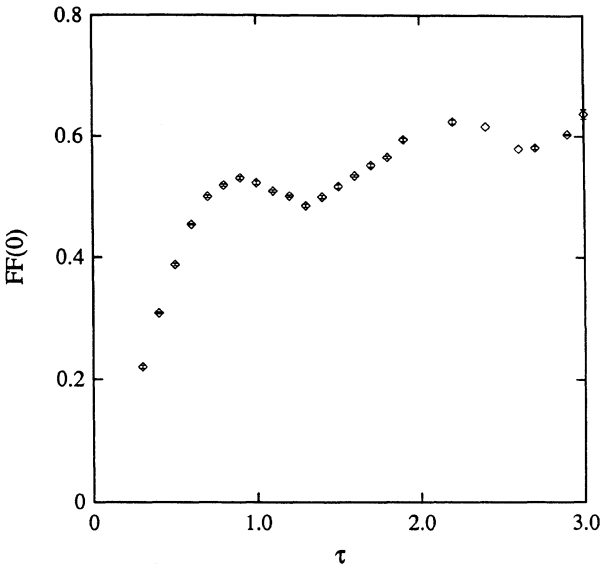

FIG. 20. Filling factor at the midplane ($z = 0$) versus optical depth, for model (iii). The filling factor reaches large values at quite low optical depths.

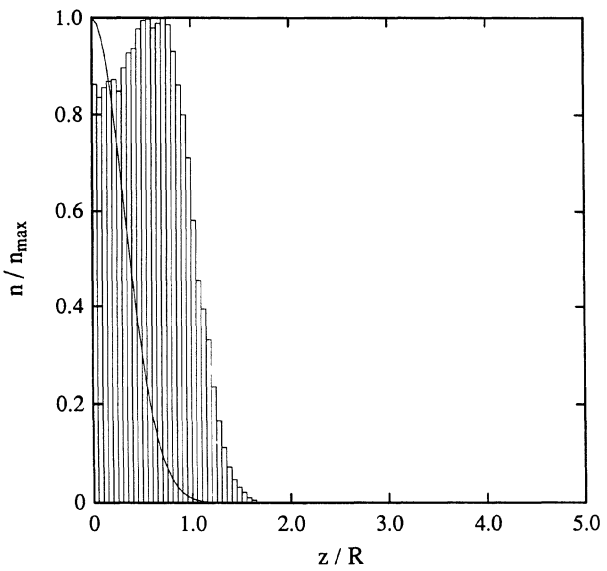

FIG. 22. Histogram of the particle number density as a function of distance from the midplane ($z = 0$), for the self-gravity model (iii) with $\tau = 0.9$. The solid line shows Eq. (21). A minimum is developing at the midplane.

in the neighborhood of $\tau = 2.2$ with magnitude $FF(0) = 0.624$.

These interesting oscillations are directly associated with an unexpected behavior of the vertical distribution function (Figs. 21–24). Figure 21 shows that at the low optical depth $\tau = 0.4$ the distribution (17) is an adequate representation of the vertical profile. Note that the ring with average self-gravity is significantly flatter than the rings without self-gravity. Since the velocity dispersions are comparable, the factor by which the vertical scale is flattened is roughly just the self-gravity enhancement factor g (see Eq. (17)). As the optical depth is increased, the vertical distribution again begins to deviate from the Gaussian profile; initially by becoming more "square." At not much larger optical depths, the vertical distribution begins to show a minimum at the midplane, $z = 0$! This is illustrated in Fig. 22 for optical depth $\tau = 0.9$, at which $FF(0)$ had its first maximum. The minimum at the midplane becomes deeper with increasing optical depth until $\tau = 1.3$, where the first minimum in $FF(0)$ occurs. The vertical distribution for $\tau = 1.3$ is shown in Fig. 23. Thus the "standard" model with self-gravity factor

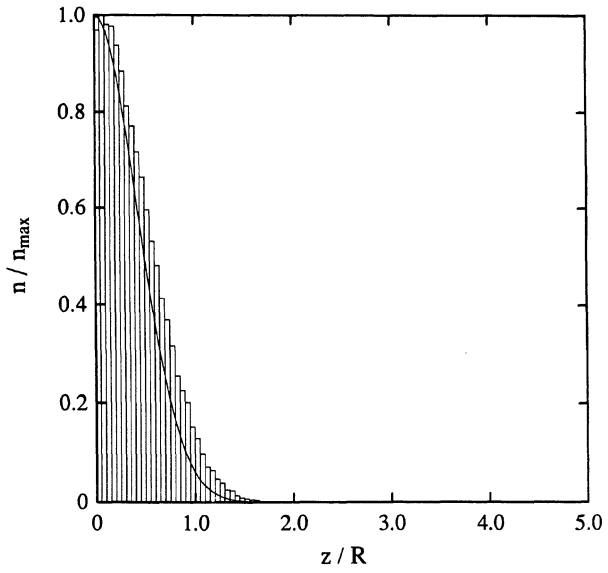

FIG. 21. Histogram of the particle number density as a function of distance from the midplane ($z = 0$), for the self-gravity model (iii) with $\tau = 0.4$. The solid line shows Eq. (21).

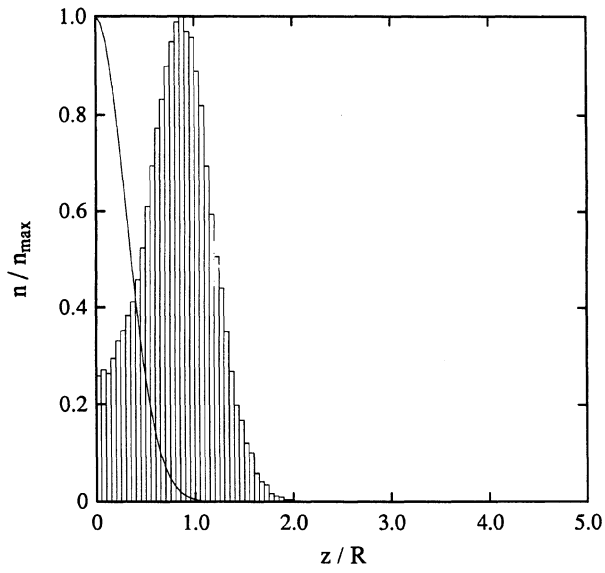

FIG. 23. Histogram of the particle number density as a function of distance from the midplane ($z = 0$), for the self-gravity model (iii) with $\tau = 1.3$. The solid line shows Eq. (21). The minimum at the midplane is fully developed. The standard ring model with self-gravity factor $g = 3.6$ develops vertically stratified layers or sheets.

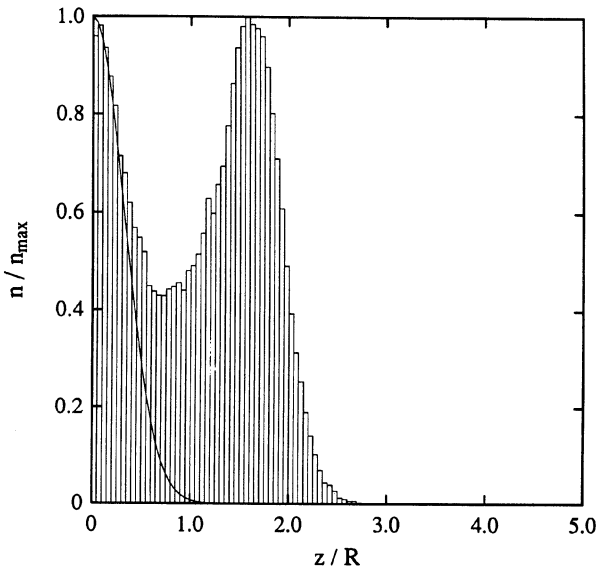

FIG. 24. Histogram of the particle number density as a function of distance from the midplane ($z = 0$), for the self-gravity model (iii) with $\tau = 1.9$. The solid line shows Eq. (21). At $\tau = 1.9$, the equilibrium configuration of the standard ring model with self-gravity is three well-defined sheets lying on top of one another.

$g = 3.6$ forms vertically stratified layers or sheets above an optical depth of about unity. As the optical depth is further increased the minimum at $z = 0$ begins to fill, but as it does so a new minimum appears near $z \approx R$. Figure 24 shows the vertical distribution for $\tau = 1.9$. At $\tau = 1.9$, the equilibrium configuration of the standard ring model is three well-defined sheets lying on top of one another. It is perhaps not surprising now that as the optical depth is further increased more and more layers are formed; we have seen up to six well-defined layers by $\tau = 3$.

We have verified that the formation of these layers is not an artifact of a commensurability between the particle size and the unit-cell size by performing simulations for optical depth $\tau = 1.3$ with different numbers of particles and thus different sizes for the unit cell. The original simulation used $N = 40$; the two auxiliary simulations used $N = 10$ and $N = 20$. All three vertical distributions are in excellent agreement. This is a further illustration that $N = 40$ was a conservative choice.

Similar layers were found by Campbell and Brennan (1985) in a numerical simulation of two-dimensional Couette flow of rough inelastic disks.

While the formation of layers is not an artifact of the simulation, it is clear that the layers are likely to be related to the assumption that all particles have the same size, since the spacing of the layers is of order twice the particle radius. With a more realistic distribution of particle sizes, the well-defined layers will most likely disappear. There may, however, be some remnant of this phenomenon. For example, it may be that particles in one layer do not often switch to the other layer, i.e., there may not be vertical mixing. This effect could persist with a distribution of particle sizes.

While it is beyond the realm of physical applicability, it is nevertheless interesting to push the optical depth to higher values to see if there is anything similar to the phase transition suggested by AT. It turns out that a phase transition of sorts does occur in our case (iii) simulation for optical depth $\tau = 2.9$. The vertical distribution function shows seven maxima. Closer examination reveals that in this case layers are not formed, but instead the particles projected on the xz plane form a regular lattice, with alternately four particles across the ring vertically, then three particles, then four, etc. There has been a limited "crystallization." The particles still maintain the mean shear flow. This is accomplished by the particles streaming in the y direction along the crystal-lattice positions in the xz plane. While amusing, this phenomenon is probably artificial, since the regular lattice could not fit into our periodic cell unless the cell size was commensurate with the lattice.

f) Comparison with Haff's Theory

Haff (1983) has discussed an approximate theory for granular flow, which has been applied to planetary rings by Borderies *et al.* (1985, hereafter referred to as BGT). Haff's theory treats the ring material as incompressible, with thickness $2h$. The mean density ρ is assumed to be independent of height and related to the particle density ρ_p by $\rho = FF\rho_p$, when FF is the filling factor. The mean free path is assumed to be much less than the particle radius (cf. Fig. 18), and the nonlocal momentum transport is assumed to be much larger than local transport (cf. Fig. 13).

There are some obstacles to comparing Haff's theory with our numerical results. First, we might expect that Haff's theory would apply whenever the dominant transport mechanism was nonlocal, or when the number of collisions per orbit was, say, $\gtrsim 10$. For model (ii), these conditions are satisfied for $\tau \gtrsim 1$ (Figs. 13 and 16). However, for $\tau = 1$ the filling factor is only 0.2 (Fig. 15), and $FF(0) \gtrsim 0.4$ by $\tau = 3$. Haff's theory cannot predict the filling factor, which is needed to relate his theoretical parameters ρ and h to the input parameter τ. Thus, either we must use the results of the simulation to determine the filling factor, or we must accept an uncertainty of a factor of 2 or more in the relation between optical depth and density or ring thickness. A second obstacle is that the theory contains at least three undetermined coefficients of order unity, which weakens its predictive powers substantially. A third obstacle is that Haff's theory cannot describe layered flows of the kind seen in model (iii) at high optical depths.

Nevertheless, the limited comparisons available to us suggest that Haff's theory captures much of the physics of dense Keplerian granular flow. Haff's theory predicts that the rms velocity of the ring particles is

$$v = c_1 \Omega R, \tag{22}$$

where R is the particle radius and c_1 is a dimensionless constant of order unity. Figure 12 shows that at high optical depth the principal axes of the velocity ellipsoid approach constant values in the range 0.9–$1.3\Omega R$, suggesting that c_1 is nearly unity. The rms velocity is very similar in model (iii) (Fig. 17), confirming Haff's prediction that c_1 is independent of the enhancement factor g.

The height-averaged kinematic viscosity in Haff's theory takes the form

$$\bar{\nu} = \Omega R^2 \frac{c_2 g^2 \tau^2}{FF^2}. \tag{23}$$

Thus the ratio of the viscosity at $\tau = 1$ in model (iii) to the viscosity in model (ii) at the same optical depth should equal

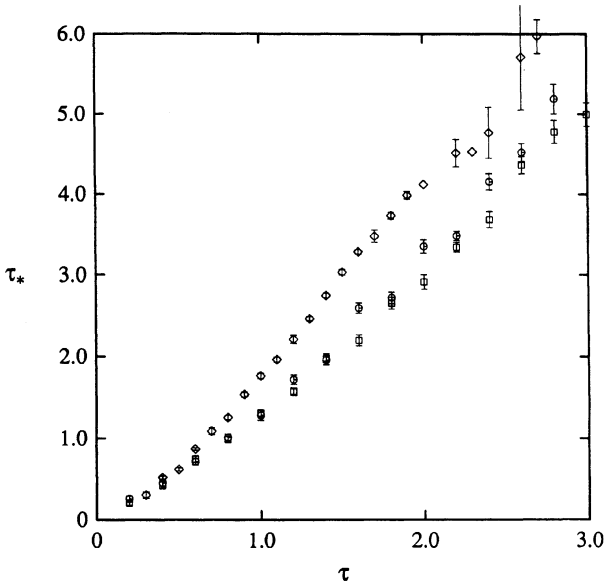

FIG. 25. Physical optical depth versus dynamical optical depth, for the three models (model (i)—squares, model (ii)—circles, model (iii)—diamonds).

the ratio of $(g/FF)^2$ in the two models. The simulations show that both ratios are $\simeq 3$, in good agreement with the prediction. The theory also predicts that $\bar{\nu} \propto \tau^2$. Fitting the results of model (ii) over the range $2 < \tau < 3$, we find $\bar{\nu} \propto \tau^{\alpha}$, with $\alpha = 1.2$, which is too low. Part of the discrepancy is removed if we account for the increase in filling factor between $\tau = 2$ and $\tau = 3$, thereby raising the best-fit exponent to 1.7, which is in adequate agreement.

g) Optical Depth

The relationship between the physical optical depth τ_* and the dynamical optical depth τ has been determined by shooting skewers through the simulation. The physical optical depth is defined so that $\exp(-\tau_*)$ is the average fraction of skewers that penetrate the ring without piercing any particles. The results of the simulations for all three models are shown in Fig. 25. At very low optical depths, the two optical depths are very nearly the same for all models, but at higher optical depths the physical optical depth is larger than the dynamical optical depth.

V. CONCLUSIONS

We have described a novel numerical technique for studying the dynamics of differentially rotating particle disks. Our technique is closely related to the methods of non-equilibrium molecular dynamics (Evans and Morriss 1984) and is based on the examination of the dynamics of particles in a small patch of the ring and the use of shearing periodic boundary conditions.

We have concentrated on the behavior of the standard model of particulate disks, in which all particles are smooth, inelastic spheres of a single radius and detailed gravitational interactions between the particles are ignored.

We have compared our numerical results with two kinetic theories of the standard model. Goldreich and Tremaine (1978) determined the equilibrium properties of a dilute (low filling factor) particle disk using the Boltzmann equation, and Araki and Tremaine (1986) generalized the Goldreich and Tremaine results to dense rings using the Enskog approximation.

We find that:

(1) The Goldreich–Tremaine theory correctly predicts the critical coefficient of restitution as a function of optical depth. Rings containing particles that are more elastic than this critical coefficient are unstable and their thickness increases exponentially. Rings with a small coefficient of restitution collapse until either the coefficient of restitution increases due to the lower impact velocities or the filling factor is no longer small.

(2) In the cases we examined, the Goldreich–Tremaine model predicts the orientation of the velocity ellipsoid well (up to $\tau \lesssim 3$); it predicts the axis ratios of the velocity ellipsoid less well (errors of up to 20% by $\tau = 3$), and does not adequately predict the viscosity for $\tau \gtrsim 0.3$, mainly because it neglects nonlocal viscous effects.

(3) The Araki–Tremaine model provides improved predictions for the axis ratios of the velocity ellipsoid and far better predictions for the viscosity than the Goldreich–Tremaine model (see Fig. 13).

(4) There is no evidence for a viscous instability in any model that we have examined.

(5) When the midplane filling factor $FF(0)$ exceeds $\simeq 0.5$ (the freezing point of a static fluid of elastic hard spheres), the disk particles organize themselves into two or more horizontal layers or sheets. Thus each particle tends to remain on one side of the midplane, in contrast to dilute rings, in which the particles spend half of their time on each side of the midplane.

The standard model is a grossly oversimplified model of planetary rings. Effects such as tangential friction, particle-size distribution, and gravitational interactions between particles are all likely to be present in real rings and may have an important influence on the equilibrium dynamics. All of these effects can be incorporated in our numerical simulation, although at increased computational cost.

So far, our simulations show no evidence of a liquid–solid phase transition, nor do they provide any clues to the origin of the fine-scale structure in the B ring. It will be interesting to extend our calculations to examine the behavior of a ring with a broad particle-size distribution, since the formation of layered sheets at high optical depth is more difficult in this situation.

We thank Jeff Bishop, Charles Campbell, Peter Goldreich, and Alar Toomre for discussions and thoughtful criticism. This research was supported by NSF grant AST-8412365, by an NSERC operating grant, and by a Special Research Grant from the Connaught Fund at the University of Toronto.

REFERENCES

Araki, S. (1987). Private communication.
Araki, S., and Tremaine, S. (1986). Icarus **65**, 83.
Borderies, N., Goldreich, P., and Tremaine, S. (1985). Icarus **63**, 406.
Brahic, A. (1977). Astron. Astrophys. **54**, 895.
Brahic, A., and Hénon, M. (1977). Astron. Astrophys. **59**, 1.
Bridges, F. G., Hatzes, A., and Lin, D. N. C. (1984). Nature **309**, 333.
Campbell, C. S. (1986). *Tenth National Congress on Applied Mechanics*, Austin, Texas.

Campbell, C. S. (1985). J. Fluid Mech. **151**, 167.
Evans, D. J., and Morriss, G. P. (1984). Comput. Phys. Rep. **1**, 297.
French, R. G., Elliot, J. L., French, L. M., Kangas, J. A., Meech, K. J., Ressler, M. E., Buie, M. W., Frogel, J. A., Holberg, J. B., Fuensalida, J. J., and Joy, M. (1987). Icarus (submitted).
Goldreich, P., and Tremaine, S. (1978). Icarus **34**, 227.
Haff, P. K. (1983). J. Fluid. Mech. **134**, 401.
Hill, G. W. (1978). Am. J. Math. **1**, 5.
Julian, W. H., and Toomre, A. (1966). Astrophys. J. **146**, 810.
Lees, A. W., and Edwards, S. F. (1972). J. Phys. C **5**, 1921.
Lin, D. N. C., and Bodenheimer, P. (1981). Astrophys. J. Lett. **248**, L83.
Lukkari, J. (1981). Nature **292**, 433.
Maxwell, J. C. (1857). Letter to William Thomson, reproduced in *Maxwell on Saturn's Rings*, edited by S. G. Brush, C. W. F. Everitt, and E. Garber (1983; MIT, Cambridge).
Petit, J.-M., and Hénon, M. (1987). Astron. Astrophys. **173**, 389.
Salo, H. (1987). Icarus **70**, 37.
Ward, W. R. (1981). Geophys. Res. Lett. **8**, 641.